

## Article

# Seismic Performance Analysis of Corrugated Steel Plate Shear Wall Connected with Beams Only

Qiang Cao <sup>1</sup>, Jingyu Huang <sup>2,3,\*</sup> and Baonan Gu <sup>1</sup>

<sup>1</sup> College of transportation Engineering, Tongji University, Shanghai 201804, China; caoqiang6188@163.com (Q.C.); gbnyyh@163.com (B.G.)

<sup>2</sup> College of Civil Engineering, Tongji University, Shanghai 200092, China

<sup>3</sup> National Maglev Transportation Engineering R&D Center, Tongji University, Shanghai 201804, China

\* Correspondence: huangjingyu@tongji.edu.cn

**Abstract:** This paper studied the seismic performance of corrugated steel plate shear walls with vertical corrugated steel plates connected with beams only (CboSPSWs). A numerical model of a CboSPSW was developed. Then, a series of parametric analyses were conducted to determine the effects of the related parameters on the hysteretic performance of CboSPSWs, including the height–thickness ratio, aspect ratio, corrugation angle, stiffness of the free-edge stiffener, and surrounding frame stiffness. In addition, the limit of the stiffness of the free-edge stiffener of the CboSPSW was investigated. Finally, the serviceability of the existing design method, the Plate-Frame Interaction model (PFI), for CboSPSWs was examined. The results show that CboSPSWs have high values of strength and initial stiffness as well as good and stable energy dissipation capacities. The ultimate strength of the corrugated steel plate (CSP) can be improved significantly by free-edge stiffeners. When the flexural stiffness ratio exceeds 1.0, the increase of the average stress of the CSPs close to the beams is less than 20%, and the tension field develops fully in the CSPs in CboSPSWs. The PFI model can predict the shear strength and initial stiffness values of the hysteretic curves of CboSPSWs with good accuracy, which can be used in the design and plastic analyses of CboSPSWs.

**Keywords:** corrugated steel plate shear wall; tension field; PFI model; corrugated steel plate; free-edge stiffener



**Citation:** Cao, Q.; Huang, J.; Gu, B.

Seismic Performance Analysis of Corrugated Steel Plate Shear Wall Connected with Beams Only.

*Buildings* **2023**, *13*, 2220. <https://doi.org/10.3390/buildings13092220>

Academic Editors: Humberto Varum and Hiroshi Tagawa

Received: 14 July 2023

Revised: 9 August 2023

Accepted: 25 August 2023

Published: 31 August 2023



**Copyright:** © 2023 by the authors. Licensee MDPI, Basel, Switzerland. This article is an open access article distributed under the terms and conditions of the Creative Commons Attribution (CC BY) license (<https://creativecommons.org/licenses/by/4.0/>).

## 1. Introduction

Flat steel plate shear walls (FSPSWs) have been widely used in the lateral force resistance systems of multi-story and high-rise building structures [1–3]. When infilled plates are replaced with corrugated steel plates, corrugated steel plate shear walls with vertical corrugated steel plates connected with beams only (CboSPSWs) are formed. CboSPSWs have several tangible benefits. The shear strengths of the infilled plates are improved significantly without increasing the thickness of the infilled plates owing to the corrugated sections of the corrugated steel plates (CSPs). Layouts and openings for shear wall structures can be designed and adjusted with more flexibility by changing the CSP width compared to the corrugated steel plate shear walls with connections on four sides (connected with beams and columns) [4–7], and CboSPSWs (connections on two sides) can reduce the construction times and costs of shear walls. In addition, CboSPSWs can reduce the anchoring forces on columns from CSPs and the requirements of the surrounding columns. However, studies on the seismic performances of CboSPSWs under lateral loads are limited. Therefore, it is imperative to study the seismic performances of CboSPSWs under lateral loads for the design and application of shear walls.

Many researchers have studied the static and seismic performances of corrugated steel plate shear walls with corrugation laid horizontally (ChSPSWs) with experimental and numerical investigations [8–10]. The effects of various geometric parameters on the buckling strength and post-buckling behavior of CSPs were investigated [11–14]. According

to the differences in the buckling modes of CSPs, the ChSPSWs with different geometric parameters showed three buckling modes: the yielding, interactive, and elastic buckling of CSPs [15]. The ChSPSWs with elastic buckling of CSPs buckled in the early loading stages, and the behavior of the CSPs after buckling was a concerning issue [15,16]. With an increase in the thickness of the CSPs, the ChSPSWs showed interactive buckling of the CSPs [17]. The interactive buckling and the ultimate strength after the buckling of CSPs were research highlights in the shear walls [18]. In order to avoid the buckling of CSPs, ChSPSWs with properly designed geometric parameters of CSPs were investigated [19,20]. The results showed that the CSPs could avoid elastic and interactive buckling by adjusting their parameters. In addition, setting stiffeners on the CSPs was another effective way to improve the elastic buckling strength of CSPs in the ChSPSWs [21]. Besides these, the seismic performance of the ChSPSWs with openings were investigated. The ultimate capacity of CSPSWs with openings was predicted using linear regression analysis [22].

Studies on the structural performances of steel plate shear walls with corrugation laid vertically (CvSPSWs) are limited and have focused on the static performances of the shear walls. Parametric analyses were performed to determine the effects of related parameters on the structural performances of shear walls with connections on four sides [16,23,24]. The effects of vertical loads on the strengths of CvSPSWs with connections on four sides were determined with numerical simulations [25]. The elastic buckling strength of the CvSPSW was investigated based on the minimum potential energy theory [26]. The research on the CvSPSW mainly focused on the parametric analyses, and the loading mechanism and analysis methods were rarely involved. Besides the studies on CvSPSWs with connections on four sides, few studies of CboSPSWs have been carried out to investigate the parameters' effects on the structural performances of the shear walls [27,28]. In the studies on the load transfer path, failure modes of the CboSPSWs were not fully investigated. Besides these, the artificial intelligence methods developed well and rapidly, and the artificial intelligence methods possess potential advantages to seismic performance analyses of building structures [29–33].

As presented above, extensive research has been conducted on the structural performance of ChSPSWs, including the buckling strength, ultimate strength, failure modes, and behavior after the buckling of CSPs, and there are limited studies on the shear and seismic performances of CvSPSWs. However, the studies on the seismic performance of CboSPSWs are limited, and the loading mechanism, failure modes, and analysis methods of the CboSPSWs with free-edge stiffeners are not described clearly. In light of the above advantages of CboSPSWs, this paper investigated the seismic behavior of CboSPSWs with free-edge stiffeners under seismic loads. The effects of related parameters on the seismic performance were evaluated. The loading mechanism and the failure modes of the CboSPSWs with different parameters were investigated. In addition, the minimum stiffnesses of the free-edge stiffeners of the CboSPSW was proposed, and the existing design method for the CboSPSW was examined.

## 2. Finite Element Simulation and Verification

The seismic performance of the CboSPSW was evaluated using the finite element (FE) software ANSYS. A single-bay, one-story specimen of the CboSPSW was designed, as shown in Figure 1. In the specimen, the beams were welded to adjacent beams, and the CSPs were welded to the surrounding beams. The free edges of the CSPs were stiffened with stiffeners, and the stiffeners used were rectangular plates.

In accordance with the designed model, an FE model of the CboSPSW was developed, and the shell 181 element was adopted to simulate the performances of the columns, beams, CSPs, and stiffeners. The rigid connections between columns and beams and between CSPs and beams simulated the welded connections. The bottoms of columns were fixed, and the out-of-plane displacements of the beams and columns were constrained. Horizontal loads were applied on one end of the column. The loading protocol is shown in Figure 2. The elastic–perfectly plastic model was applied, and the corresponding von Mises yield

criterion and the associated flow rule were adopted in the model. CSP imperfections were taken into consideration in the simulation, and the imperfection value of the CSP was obtained by multiplying 1/750 of the CSP height by the results of the out-of-displacement deformation from the eigenvalue buckling of the FE model. The mesh sensitivity analyses for the FE model were carried out, shown in Figure 3. The results show that when the mesh sizes of the FE models are 40 mm × 40 mm, the results obtained by the FE model tend to be stable. The developed meshed FE model is shown in Figure 4.

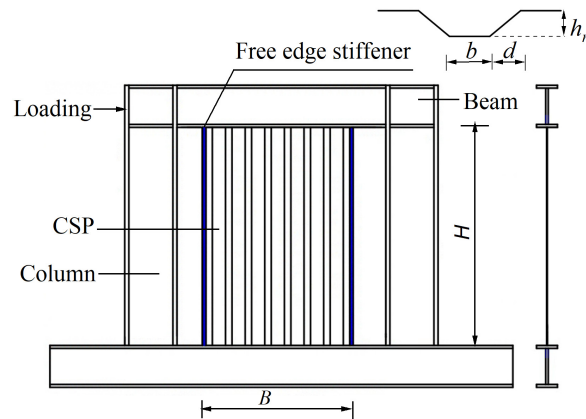


Figure 1. Diagram of a CboSPSW specimen.

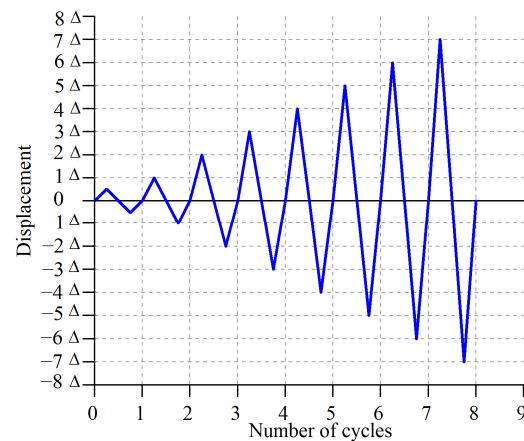


Figure 2. Loading protocol.

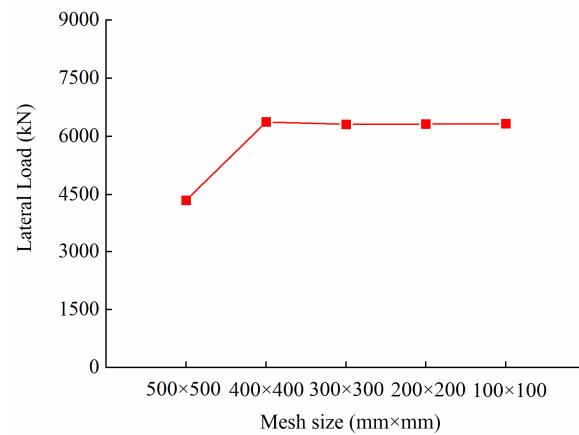
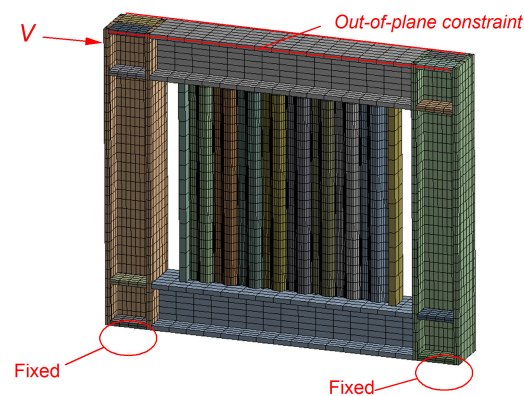


Figure 3. Mesh sensitivity analyses.



**Figure 4.** Meshed FE model of a CboSPSW.

### 2.1. FE Model Verification

The rationality and accuracy of the developed FE model were verified with a laboratory test [34]. In the test, the sections of columns were H-200 mm × 200 mm × 8 mm × 12 mm, and the top and bottom beams were H-175 mm × 175 mm × 8 mm × 10 mm and H-250 mm × 200 mm × 8 mm × 14 mm. The CSP thickness was 2.0 mm. Comparisons of the hysteretic curves and failure modes obtained from the FE model and test specimen are shown in Figures 5 and 6. From Figure 5, the ultimate load ratio of the FE model to the test specimen was 1.08, and the displacement corresponding to the ultimate load ratio of the FE model to the test specimen was 0.91. Figure 6 shows that the failure modes simulated by the FE model are compressive buckling of the column base under compression and shear loads, which are in line with that of the test. The obtained hysteretic curves and failure modes show that the developed FE model can be used to capture the seismic performance of the CboSPSW.

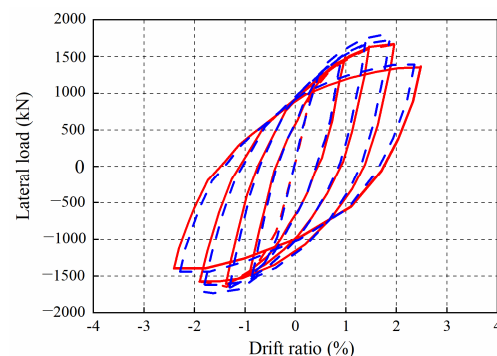


**Figure 5.** Comparison of hysteretic curves between FE model and test specimen.

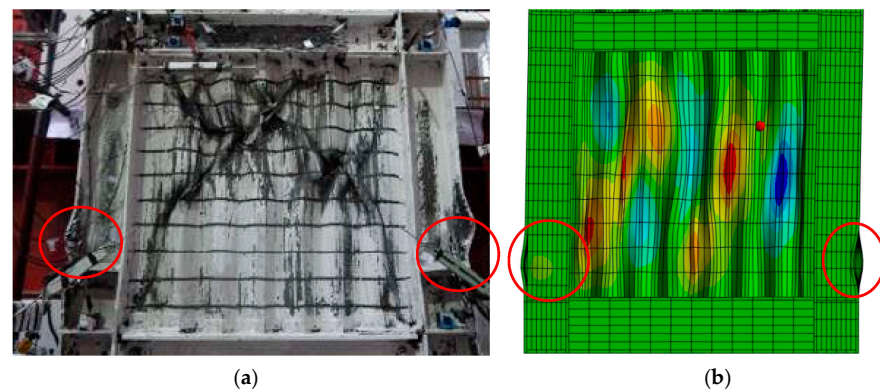


**Figure 6.** Comparison of failure modes between FE model and test specimen. (a) Test; (b) Out-of-plane deformation of FE model.

## 2.2. Dynamics Analyses

Based on the verified model, some modal analyses of the CboSPSWs were conducted to investigate the dynamic characteristics of CboSPSWs and evaluate rationality of the design of CboSPSWs.

To investigate the dynamic characteristics of the CboSPSWs, the CboSPSWs with and without free-edge stiffeners were developed. The detailed parameters of the CboSPSWs are shown in Table 1. The first six vibration modals of these models are shown in Figures 7 and 8. The first six vibration modals of the CboSPSW without free-edge stiffeners were free edge deformation, free edge deformation, lateral displacement, free edge deformation, free edge deformation, and free edge deformation, as shown in Figure 7. From Figure 8, the first six vibration modals of the CboSPSW with free-edge stiffeners were out-of-plane deformation, lateral displacement, out-of-plane deformation, free edge deformation, free edge deformation, and out-of-plane deformation. It was indicated that the free edge stiffener can avoid the free edge deformation before out-of-plane deformation of CSPs and lateral displacement of the shear wall. Besides these, the first natural frequency of the first vibration modals of the CboSPSW with free edge stiffeners were close to that of the second vibration modal.

**Table 1.** Geometric characteristics of CboSPSWs.

Stiffener Section Size (mm × mm)	$t_w$ (mm)	$H$ (mm)	$B$ (mm)	$h_r$ (mm)	$b$ (mm)	$d$ (mm)
-	10.0	3000	3100	77	110	77
300 × 40	10.0	3000	3100	77	110	77

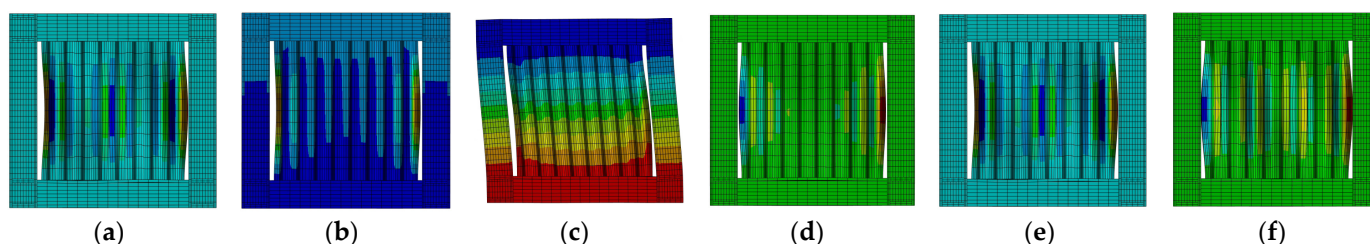


**Figure 7.** First six vibration modals and natural frequencies of the CboSPSW without free-edge stiffeners. (a) First vibration modal ( $f_1 = 51.9$  Hz); (b) 2nd vibration modal ( $f_2 = 52.8$  Hz); (c) 3rd vibration modal ( $f_3 = 55.4$  Hz); (d) 4th vibration modal ( $f_4 = 56.1$  Hz); (e) 5th vibration modal ( $f_5 = 64.3$  Hz); (f) 6th vibration modal ( $f_6 = 71.5$  Hz).

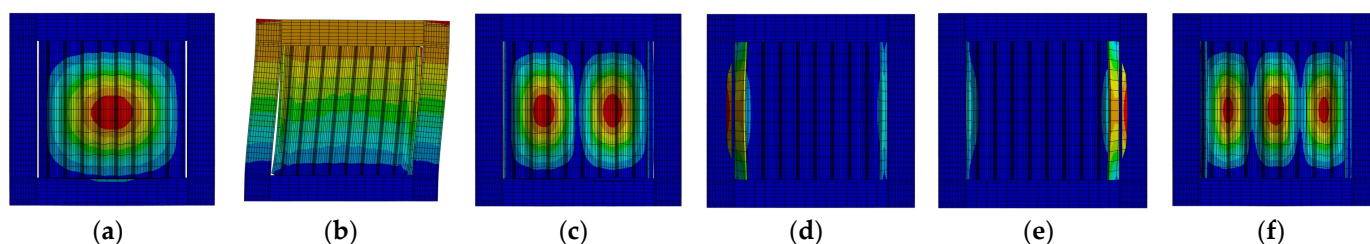


**Figure 8.** First six vibration modals and natural frequencies of the CboSPSW with free-edge stiffeners. (a) First vibration modal ( $f_1 = 54.5$  Hz); (b) 2nd vibration modal ( $f_2 = 56.7$  Hz); (c) 3rd vibration modal ( $f_3 = 62.7$  Hz); (d) 4th vibration modal ( $f_4 = 66.3$  Hz); (e) 5th vibration modal ( $f_5 = 66.6$  Hz); (f) 6th vibration modal ( $f_6 = 71.5$  Hz).

## 3. Parametric Analyses and Discussions

In this section, based on the verified model, a series of parametric analyses were carried out to investigate the related parameters' effects on the seismic performances of CboSPSWs, including the height–thickness ratio, aspect ratio, corrugation angle, stiffness of free-edge stiffeners, and surrounding frame stiffness.

### 3.1. Effect of Height–Thickness Ratio

Six specimens with different height–thickness ratios  $\lambda$  (200, 300, 400, 500, 600, and 700) were developed to investigate the effect of the height–thickness ratio on the seismic performances of CboSPSWs. The corresponding thicknesses of the CSPs  $t_w$  were 30.0, 15.0, 7.5, 6.0, 5.0, and 4.3 mm, respectively. The CSP heights of these models  $H$  were 3100, CSP width 3000 mm, corrugation depth  $h_r$  77 mm, horizontal projection of the inclined panel width  $d$  77 mm. The other parameters remained unchanged. The geometric parameters of these models are shown in Table 2. The hysteretic curves and skeleton curves are shown in Figures 9 and 10.

**Table 2.** Geometric parameters of CboSPSWs.

$t_w$ (mm)	$\lambda$	$H$ (mm)	$B$ (mm)	$d$ (mm)	$h_r$ (mm)
15.0, 10.0, 7.5, 6.0, 5.0, 4.3	200, 300, 400, 500, 600, 700	3100	3000	77	77

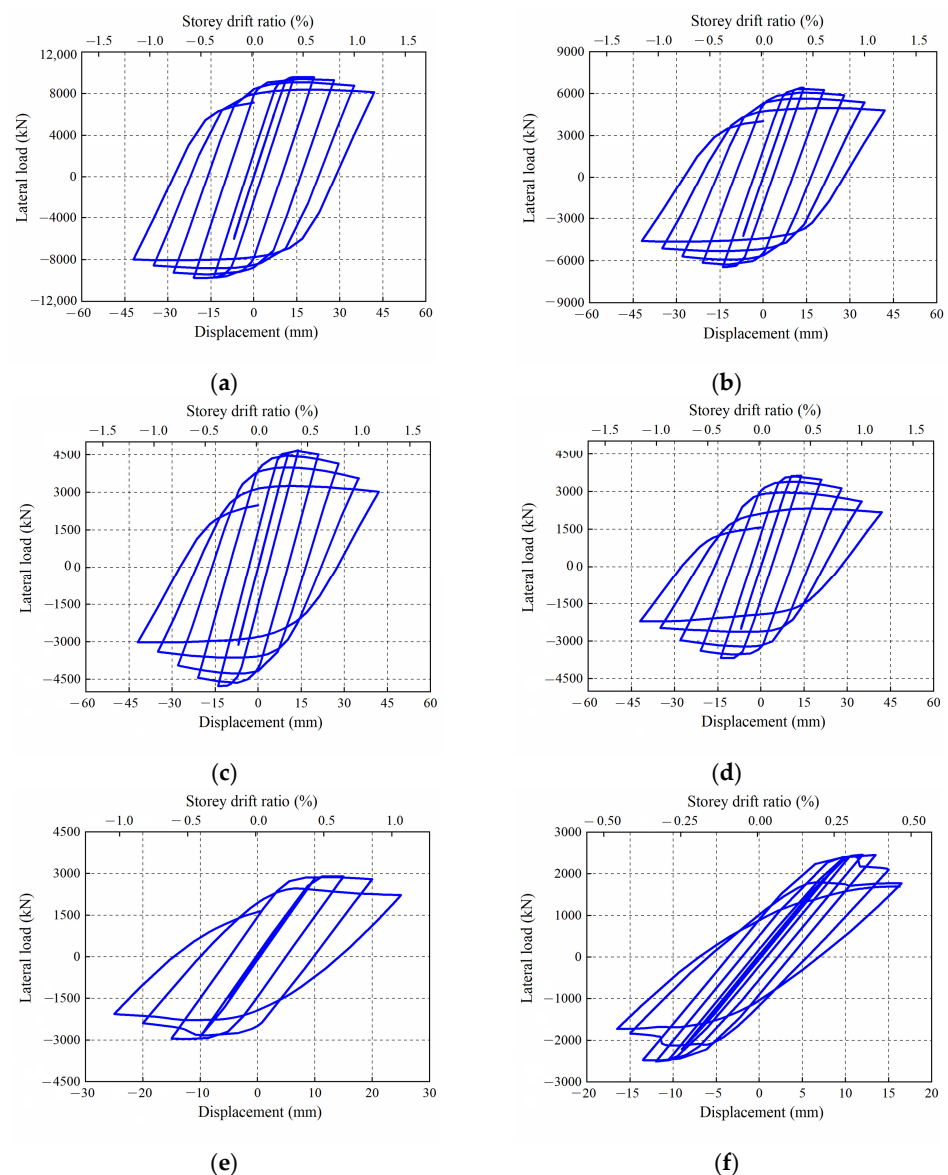


**Figure 9.** Hysteretic curves of CboSPSWs with different height–thickness ratios. (a)  $\lambda = 200$ ; (b)  $\lambda = 300$ ; (c)  $\lambda = 400$ ; (d)  $\lambda = 500$ ; (e)  $\lambda = 600$ ; (f)  $\lambda = 700$ .

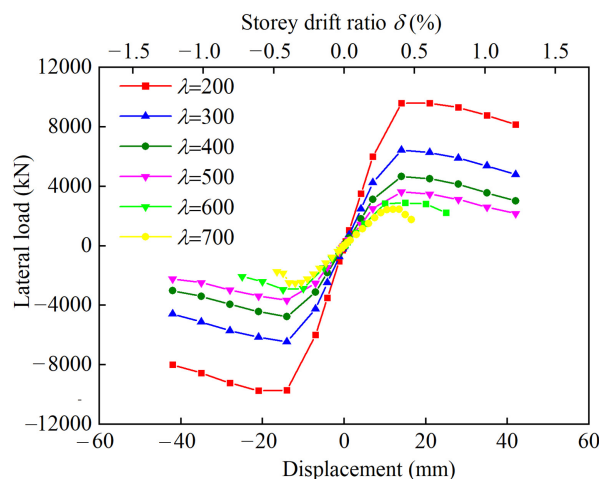


Figure 10. Skeleton curves of CboSPSWs with different height–thickness ratios.

Figure 9 shows that the hysteresis curves of the CboSPSWs are spindle-shaped. With a decrease in the height–thickness ratio, the shapes of these hysteresis curves became much fuller. It is noted that a pinching phenomenon and strength degradation occurred in the curve of the shear wall with a height–thickness ratio of 700. The ultimate shear stress of the shear wall with a height–thickness ratio of 700 was 170.5 Mpa, which was lower than the critical value of the elastic buckling stress of the CSPs ( $0.8\tau_y$ ). The buckling mode of the CSP in the CboSPSW with a height–thickness ratio of  $\lambda = 700$  was the elastic buckling of the CSP. The CSP buckled in the early loading stages and then continued to resist a greater lateral load with a tension field. The hysteretic curve was similar to that of an FSPSW or a thin ChSPSW [16]. When the height–thickness ratios were 300–600, the ultimate shear stresses of the CSPs varied from 191.7 to 208.2 Mpa, and the buckling mode of the models was the inelastic buckling of CSPs. In addition, there was no obvious pinching phenomenon or strength degradation. The shapes of these models were much fuller than those of FSPSWs and thin ChSPSWs. This was because the compressive strength of CSPs cannot be ignored due to the corrugation of CSPs. When the height–thickness ratio was 200, the ultimate stress of the CSP reached the yield strength, and the manner that the CboSPSW resisted the lateral load relied on pure shear, as shown in Figures 10 and 11.

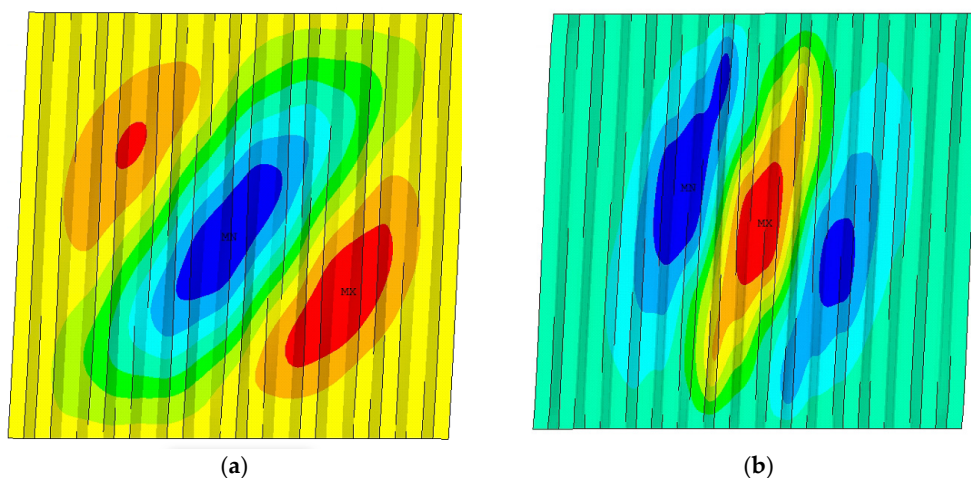


Figure 11. Failure modes of CboSPSWs with different height–thickness ratios. (a)  $\lambda = 200$ ; (b)  $\lambda = 700$ .

The corresponding failure modes of the CSPs in the CboSPSWs with height–thickness ratios of  $\lambda = 200$  and 700 are shown in Figure 11. The inclination angles of the tension

fields of the CSPs were about 60°, and the tension field of the CSP with λ = 200 developed much more fully than that of the CSP with λ = 700.

The ductility coefficient μ is also an effective indicator of the deformation capacity of shear walls [34]. The ductility coefficient μ is the ratio of the displacement corresponding to the ultimate load (Δ<sub>u</sub>) to the yield displacement (Δ<sub>y</sub>), which can be expressed as:

$$\mu = \frac{\Delta_u}{\Delta_y} \tag{1}$$

The detailed results of the ductility coefficients are shown in Table 3. From Table 3, the ductility coefficients of the CboSPSWs were 1.94, 1.54, 1.55, 1.48, 1.30, and 1.26 when the height–thickness ratios were 200, 300, 400, 500, 600, and 700. The ductility coefficient showed a negative relationship with the increase in the height–thickness ratio. The shear walls with height–thickness ratios of 600 and 700 had bad plastic deformation capacities under seismic loads.

Table 3. Results of CboSPSWs with different thickness ratios.

λ	Yield Displacement Δ <sub>y</sub> (mm)	Yield Load V <sub>y</sub> (kN)	Ultimate Displacement Δ <sub>u</sub> (mm)	Ultimate Load V <sub>u</sub> (kN)	Ductility Coefficient μ
200	10.7	9213	17.9	9755.2	1.95
300	9.1	5522	14.0	6453.4	1.54
400	9.0	4022	14.0	4769.5	1.55
500	8.8	3147	13.1	3681.1	1.48
600	9.6	2814	12.4	2898.2	1.30
700	9.5	2404	12.0	2454.2	1.26

In addition, the energy dissipation coefficient E<sub>n</sub> is used to present the energy dissipation capacities of shear walls, which is the ratio of the area enclosed by hysteretic curves (A<sub>h</sub>) to the elastic strain energy (A<sub>e</sub>) in each hysteresis loop, which can be expressed as:

$$E_n = \frac{A_h}{A_e} \tag{2}$$

The energy dissipation coefficients E<sub>n</sub> of the CboSPSWs with different height–thickness ratios are shown in Figure 12. As can be seen in Figure 12, the energy dissipation coefficients E<sub>n</sub> of the shear walls increased with the drift ratios, which indicates that the CboSPSWs had stable energy dissipation capacities. In addition, the energy dissipation coefficients of the shear walls showed opposite trends with increases in the height–thickness ratios. When the height–thickness ratio was 700, the energy dissipation coefficient E<sub>n</sub> decreased significantly. It is suggested that the height–thickness ratio should be less than 600 for stable energy dissipation in the design and application of CboSPSWs.

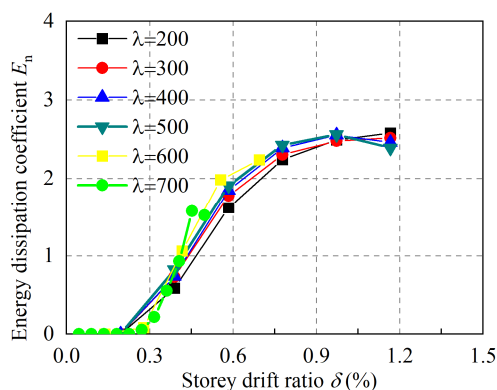


Figure 12. Energy dissipation coefficients with different height–thickness ratios.

### 3.2. Effect of Aspect Ratio

The effect of the aspect ratio on the hysteretic performances of CboSPSWs was investigated. Six CboSPSW specimens with different aspect ratios ( $B/H = 0.5, 1.0, 1.5, 2.0, 2.5,$  and  $3.0$ ) were developed, and the CSP heights remained unchanged. The geometric parameters of these models are shown in Table 4. The hysteretic curves and skeleton curves of these models are shown in Figures 13 and 14.

**Table 4.** Geometric characteristics of CboSPSWs.

$B$ (mm)	$B/H$	$\lambda$	$d$ (mm)	$h_r$ (mm)	$b$ (mm)	$H$
1500, 3000, 4500, 6000, 7500, 9000	0.5, 1.0, 1.5, 2.0, 2.5, 3.0	300	77	77	110	3100

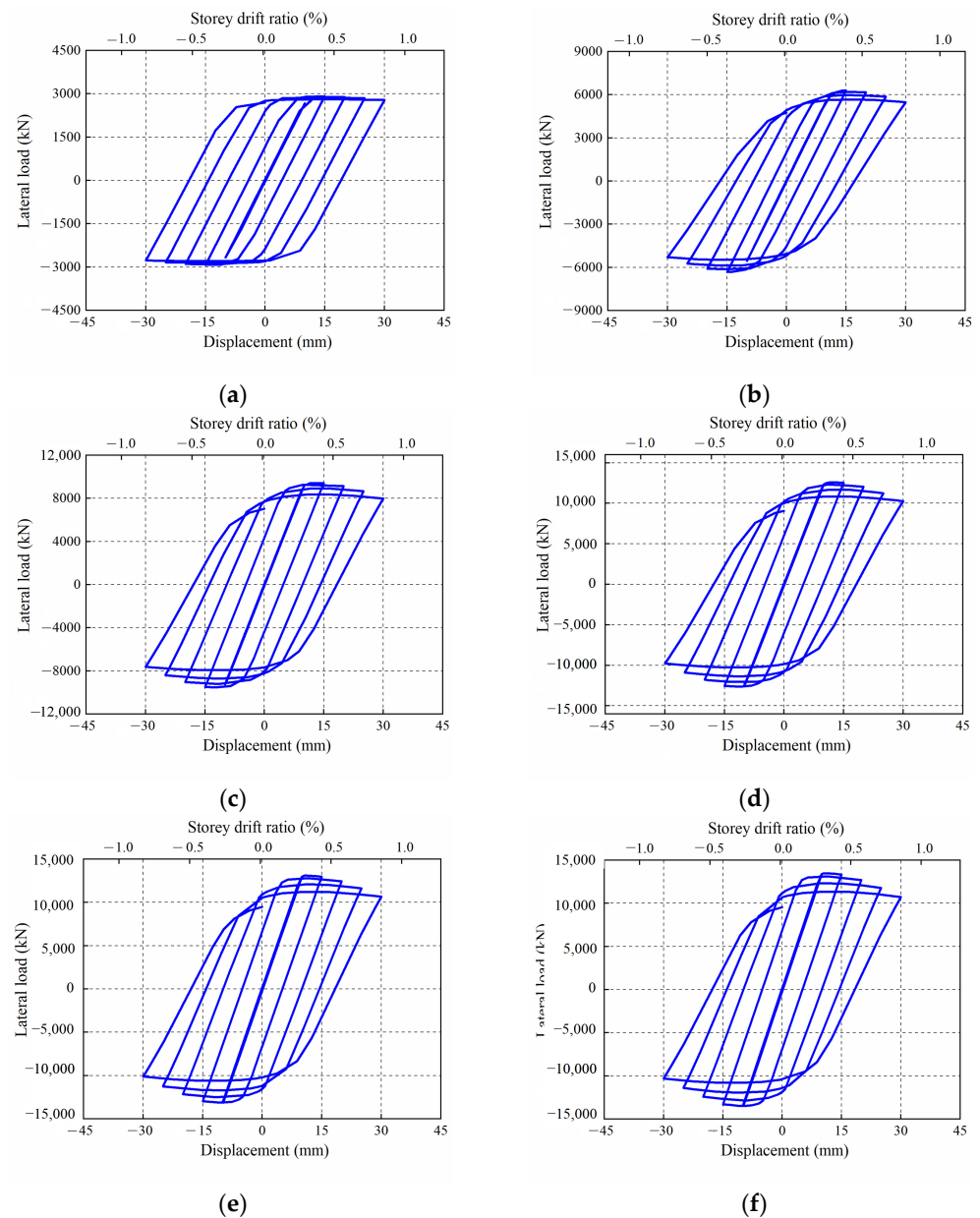


**Figure 13.** Hysteresis curves of CboSPSWs with different aspect ratios. (a)  $B/H = 0.5$ ; (b)  $B/H = 1.0$ ; (c)  $B/H = 1.5$ ; (d)  $B/H = 2.0$ ; (e)  $B/H = 2.5$ ; (f)  $B/H = 3.0$ .

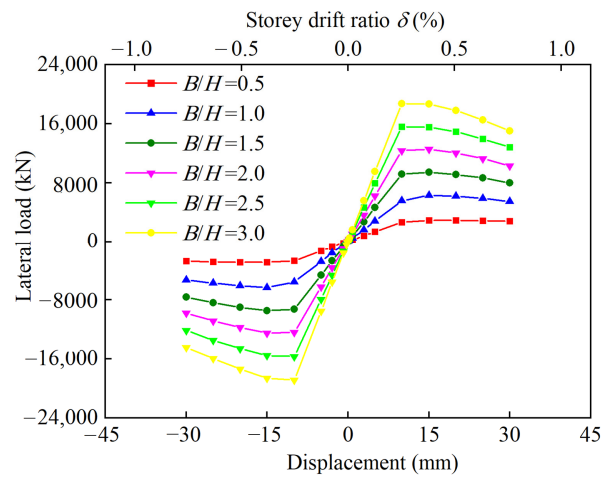


Figure 14. Skeleton curves of CboSPSWs with different aspect ratios.

Figures 13 and 14 show that there were no obvious pinching phenomena in these models and that the shear strength and initial stiffness increased with an increase in the aspect ratio. After the peak loads, the decrease rates of the strengths of the shear walls increased as the aspect ratio increased, as shown in Figure 14.

The out-of-plane deformation of the CboSPSWs with aspect ratios of  $B/H = 1.0$  and  $3.0$  are shown in Figure 15. There were three half-waves in the CboSPSW with  $B/H = 1.0$ , while there were nine half-waves in the CboSPSW with  $B/H = 3.0$ , and the inclination angles were approximately  $60^\circ$ .

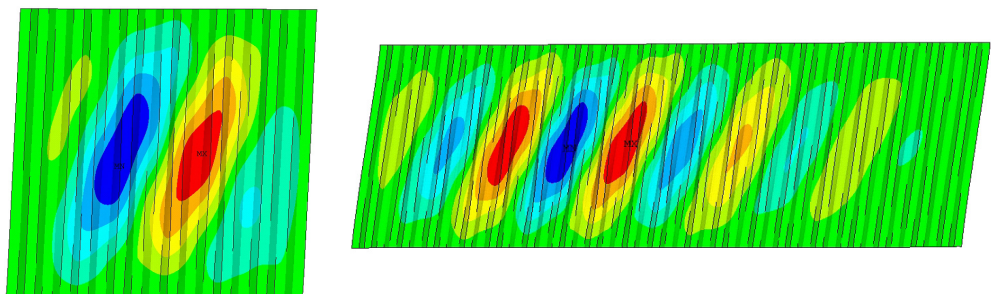


Figure 15. Out-of-plane deformation of CboSPSWs with different aspect ratios.

The curves of the energy dissipation coefficients versus the aspect ratio are shown in Figure 16. The dissipation coefficient increased with an increase in the drift ratio, which shows the shear walls had stable dissipation capacities, and the energy dissipation coefficient increased with increases in the aspect ratios when the drift ratios were fixed.

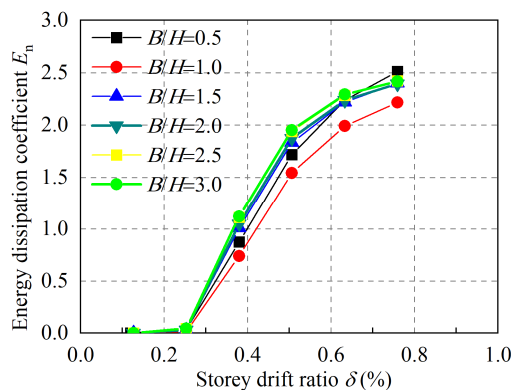


Figure 16. Energy dissipation coefficients with different aspect ratios.

### 3.3. Effect of Corrugation Angle

The corrugation angle influences the area moment of inertia and the out-of-plane stiffness of CSPs. Five specimens with different angles ( $30^\circ$ ,  $37.5^\circ$ ,  $45^\circ$ ,  $52.5^\circ$ , and  $60^\circ$ ) were established to study the effect of the corrugation angle. In these models, the corrugation angles were changed by adjusting the depths of corrugation in the CSPs, and the corresponding corrugation depths were 44, 59, 77, 100, and 133 mm. The CSP height ( $H$ ) and subpanel width ( $b$ ) remained unchanged. The detailed parameters of the CboSPSWs are shown in Table 5. Hysteresis curves and skeleton curves with various corrugation angles are shown in Figures 17 and 18.

**Table 5.** Geometric characteristics of CboSPSWs.

$\theta$	$\lambda$	$d$	$H$	$B$	$h_r$	$b$
		(mm)	(mm)	(mm)	(mm)	(mm)
$30^\circ, 37.5^\circ, 45^\circ, 52.5^\circ, 60^\circ$	300	44, 59, 77, 100, 133	3000	3100	77	110

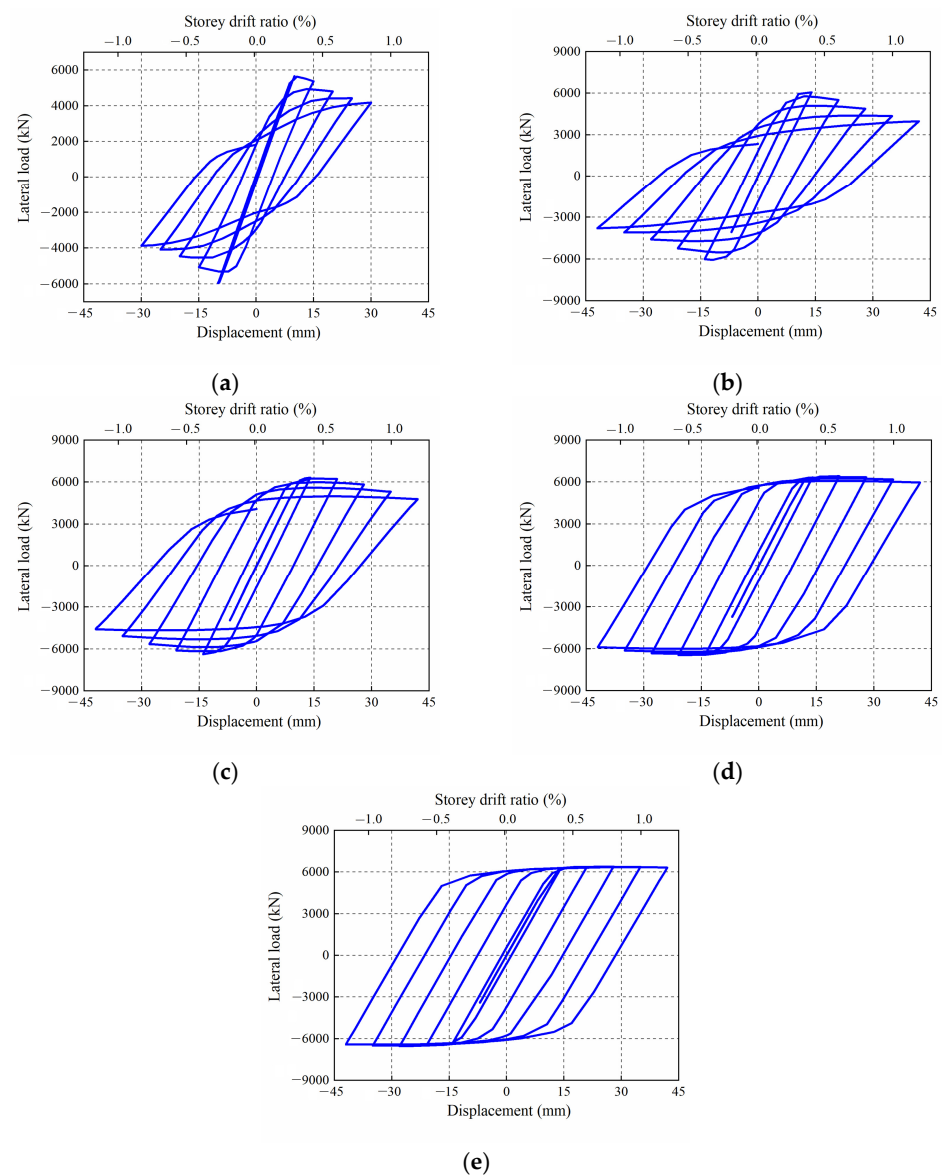


**Figure 17.** Hysteretic curves of CboSPSWs with different corrugation angles. (a)  $\theta = 30^\circ$ ; (b)  $\theta = 37.5^\circ$ ; (c)  $\theta = 45^\circ$ ; (d)  $\theta = 52.5^\circ$ ; (e)  $\theta = 60^\circ$ .

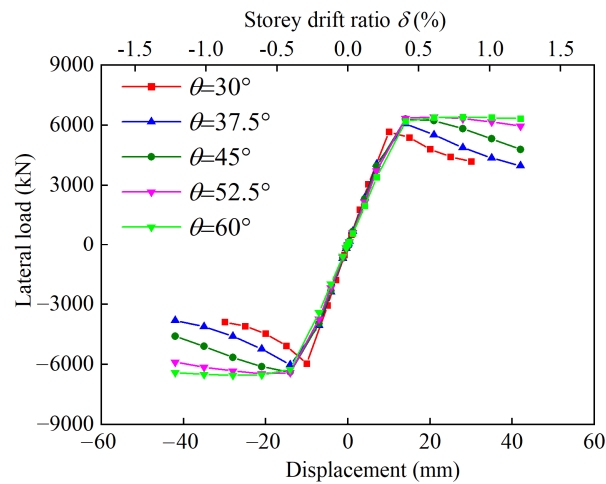


**Figure 18.** Skeleton curves of CboSPSWs with different corrugation angles.

Figure 17 shows that the shapes of the CboSPSWs became much fuller as the corrugation angles increased. The ultimate strengths of the CSPs showed a positive relationship with the corrugation angle, as shown in Figure 18. This was because the in-plane bending stiffness and out-of-plane strength increased as the corrugation depths increased. Curves of the energy dissipation coefficients versus the corrugation angle are shown in Figure 19. When the corrugation angle was  $30^\circ$ , the dissipation coefficient  $E_n$  was small, and the corresponding hysteresis loop area and the displacement ductility were small. When the corrugation angles were  $45^\circ$  and  $52.5^\circ$ , the dissipation coefficient  $E_n$  showed large and stable energy dissipation capacities and large ultimate strengths.

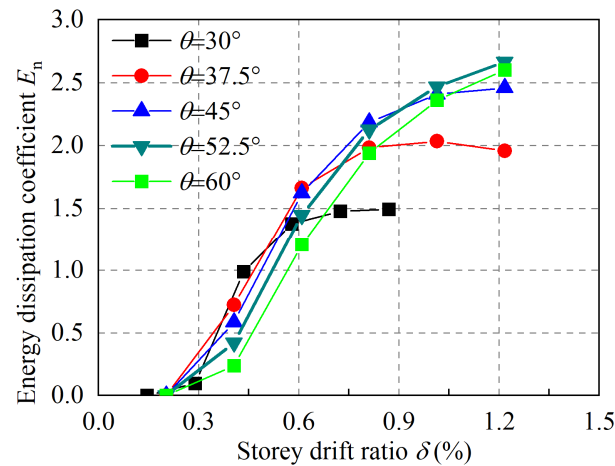


**Figure 19.** Energy dissipation coefficients with different corrugation angles.

### 3.4. Stiffness of Free-Edge Stiffeners

The stiffeners of free edges play an important part in the strength and development of tension fields in CSPs. In order to discuss the stiffness of the free-edge stiffener effect, the flexural stiffness ratio of the stiffener of the free edge to the CSP  $\eta$  is introduced, which can be expressed as:

$$\eta = \frac{2E_s I_s}{D_x H_w} \quad (3)$$

where  $E_s$  and  $I_s$  are the elastic modulus and moment of inertia of the free-edge stiffener,  $D_x$  is the sectional moment of inertia of the CSP, and  $H_w$  is the CSP height.

Figure 20 shows the mechanical behavior of the CSP with free-edge stiffeners. The areas away from the free edges are high-efficiency zones for resisting the shear loads, while the areas close to the free edges are low-efficiency zones for resisting the lateral load. The

stiffeners can provide constraints for the free-edge zones to develop tension fields to resist greater loads compared to those without edge stiffeners. When the moments of inertia of the free-edge stiffeners were calculated, the benefits of the T sections developed by the stiffeners and the connected CSPs with a length of  $15t_w$  could be taken into consideration, as shown in Figure 20.

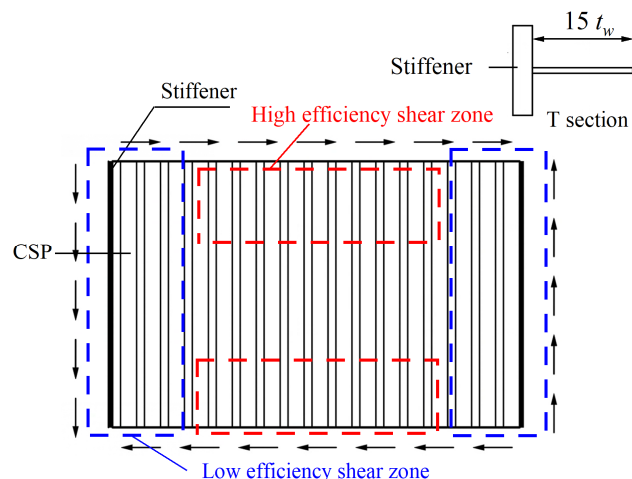


**Figure 20.** Diagram of calculation model of free-edge stiffener.

Eight CboSPSW specimens ( $\lambda = 300$ ) with different flexural stiffness ratios ( $\eta = 0, 1, 2, 3, 4, 5, 6,$  and  $7$ ) were developed. The detailed parameters of these models are shown in Table 6. Hysteresis curves and skeleton curves with different flexural stiffness ratios  $\eta$  are shown in Figures 21 and 22.

**Table 6.** Geometric characteristics of CboSPSWs.

$\eta$	$\lambda$	$H$	$B$	$h_r$	$b$	$d$
		(mm)	(mm)	(mm)	(mm)	(mm)
0, 1, 2, 3, 4, 5, 6, 7	300	3000	3100	77	110	77

From Figures 21 and 22, the shapes of the hysteretic curves became much fuller with increases in the stiffener stiffness. The buckling and ultimate strength showed a positive relationship as the edge stiffener stiffness increased. The ultimate load of the CboSPSW without edge stiffeners was 4890 kN, and the mechanical properties of the CSPs with no stiffeners were not fully utilized. The ultimate loads of the CboSPSWs with two stiffeners increased from 5563 to 6351 kN as the stiffness of the free-edge stiffeners increased. The ultimate loads of the shear walls with free-edge stiffeners were improved by 14–30%. This is because the low efficiency shear zones distribute the areas near the free edges of the CSPs show in Figure 20, and the parts of the CSPs in the low efficiency shear zones are easy to buckle and deform. With the increase of the stiffener stiffness, the free-edge stiffeners increase buckling strength and shear load of the parts of the CSPs in the low efficiency shear zones. When the flexural stiffness ratio  $\eta$  reaches 1.0, the ultimate strengths of CSPs tend to be stable. This is because the edge stiffeners can be regarded as constraints of CSPs. When the free-edge stiffeners have adequate stiffness, the tension fields of CSPs develop fully. Otherwise, the tension fields of CSPs cannot develop fully, and the mechanical properties of the CSPs in the CboSPSWs are not fully utilized. The tension fields of CSPs can also verify this phenomenon, as shown in Figure 23.

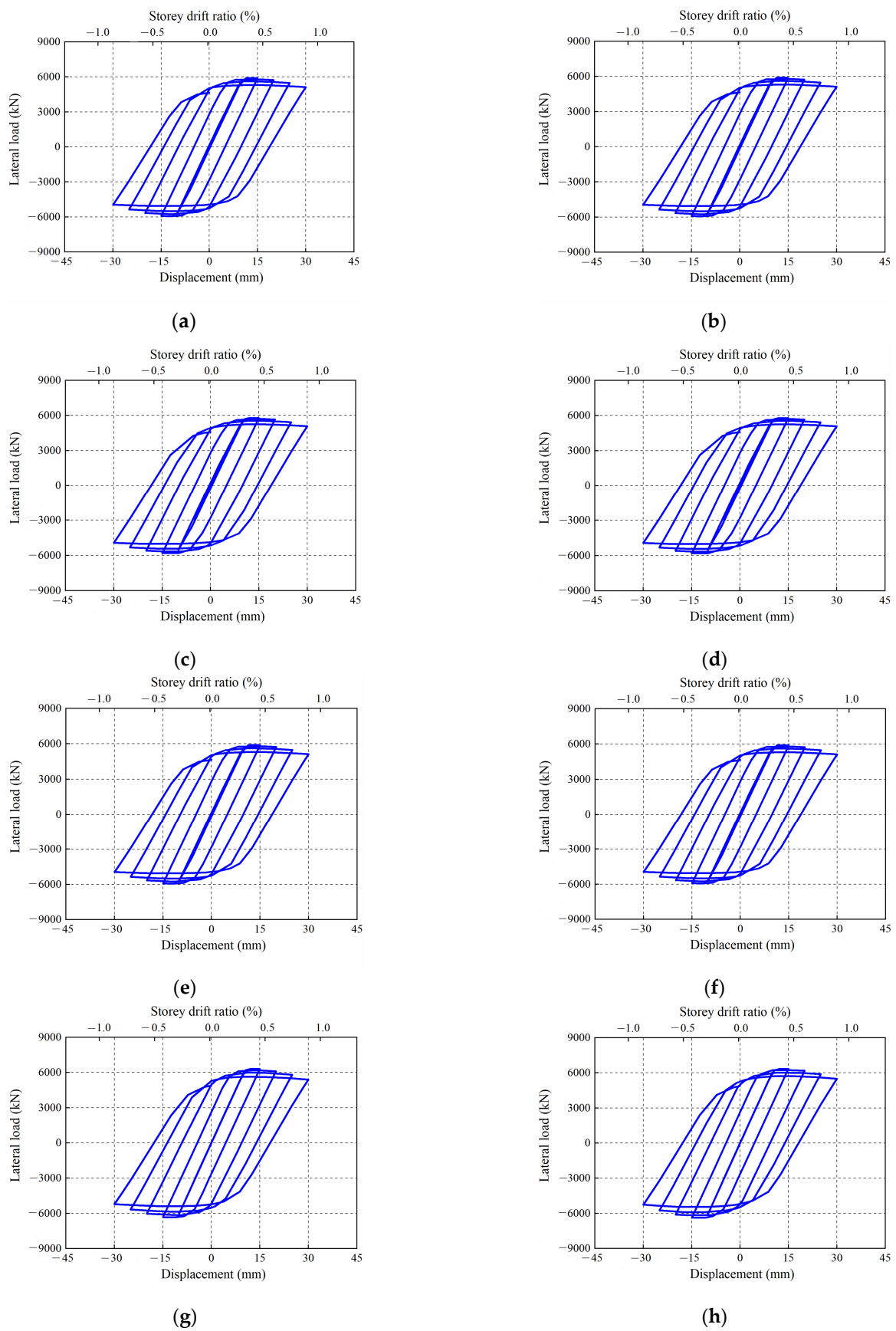


**Figure 21.** Hysteresis curves of CboSPSWs with different flexural stiffness ratios  $\eta$ . (a)  $\eta = 0$ ; (b)  $\eta = 1$ ; (c)  $\eta = 2$ ; (d)  $\eta = 3$ ; (e)  $\eta = 4$ ; (f)  $\eta = 5$ ; (g)  $\eta = 6$ ; (h)  $\eta = 7$ .

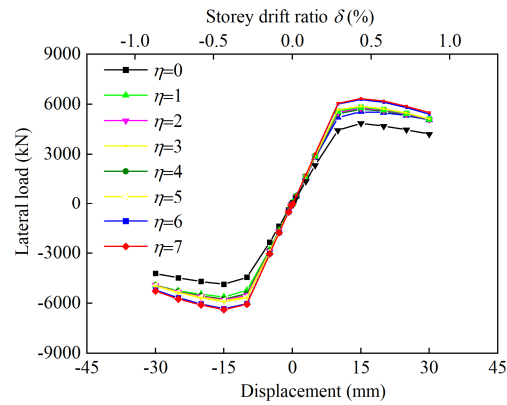


Figure 22. Skeleton curves of CboSPSWs with different flexural stiffness ratios  $\eta$ .

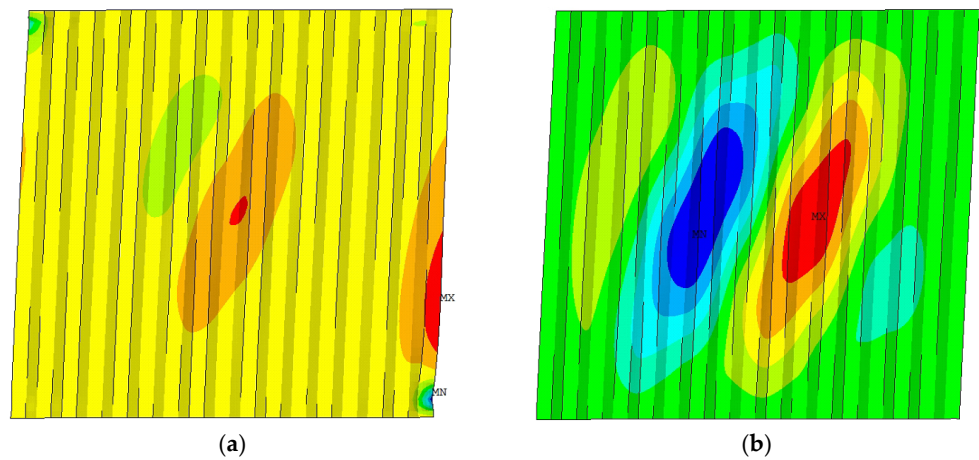


Figure 23. Failure modes of CboSPSWs with different flexural stiffness ratios  $\eta$ . (a)  $\eta = 0$ ; (b)  $\eta = 7$ .

Figure 23 shows the failure modes of CboSPSWs with different flexural stiffness ratios ( $\eta = 0$  and 7). It can be seen that the tension field of the CSP in the CboSPSW with  $\eta = 7$  developed more fully than that of the CboSPSW with  $\eta = 0$ . In addition, the CboSPSWs with free-edge stiffeners of different stiffnesses showed large and stable energy dissipation capacities, as shown in Figure 24.

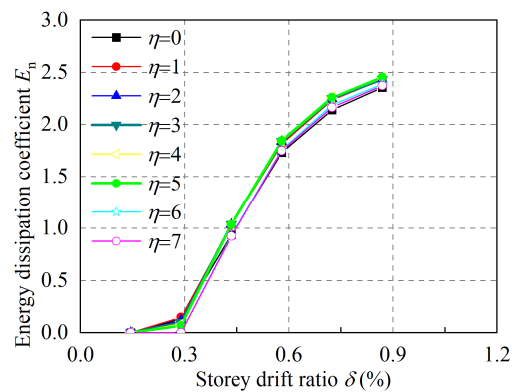


Figure 24. Energy dissipation coefficients with different flexural stiffness ratios  $\eta$ .

### 3.5. Effect of Surrounding Frame Stiffness

As the constraints of infilled plates, the minimum area moments of inertia for the beams and columns of FSPSWs were suggested in order to provide enough boundary

constraints for the tension field and buckling strength for the infilled plates of FSPSWs, which can be expressed as [35]:

$$I_{b\min} \geq 0.0031t_w B_c^4 / H_b \quad (4)$$

where  $t_w$  is the thickness of the infilled plates,  $B_c$  is the center distance between adjacent columns, and  $H_b$  is the center distance between adjacent beams.

The formation mechanism of the tension field and the boundary constraints of the infilled plates in CboSPSWs are different from those of FSPSWs. The effect of the surrounding beam stiffness on the seismic performance of the CboSPSWs is worth exploring. As stiffeners of CSPs, the surrounding beams provide constraints for CSPs in the CboSPSWs. To investigate the effect of surrounding beam stiffness on the hysteretic performance of CboSPSWs, six specimens with different surrounding beam stiffnesses ( $0.25I_{b\min}$ ,  $0.5I_{b\min}$ ,  $0.75I_{b\min}$ ,  $1.0I_{b\min}$ ,  $2.0I_{b\min}$ , and  $10.0I_{b\min}$ ) were developed. In these models, the corresponding sections of the beams were HW260 × 260 × 26 × 26, HW310 × 310 × 31 × 31, HW340 × 340 × 34 × 34, HW370 × 370 × 37 × 37, HW410 × 410 × 41 × 41, and HW650 × 650 × 65 × 65, respectively. Hysteretic and skeleton curves of CboSPSWs with various surrounding beam stiffnesses are shown in Figures 25 and 26.

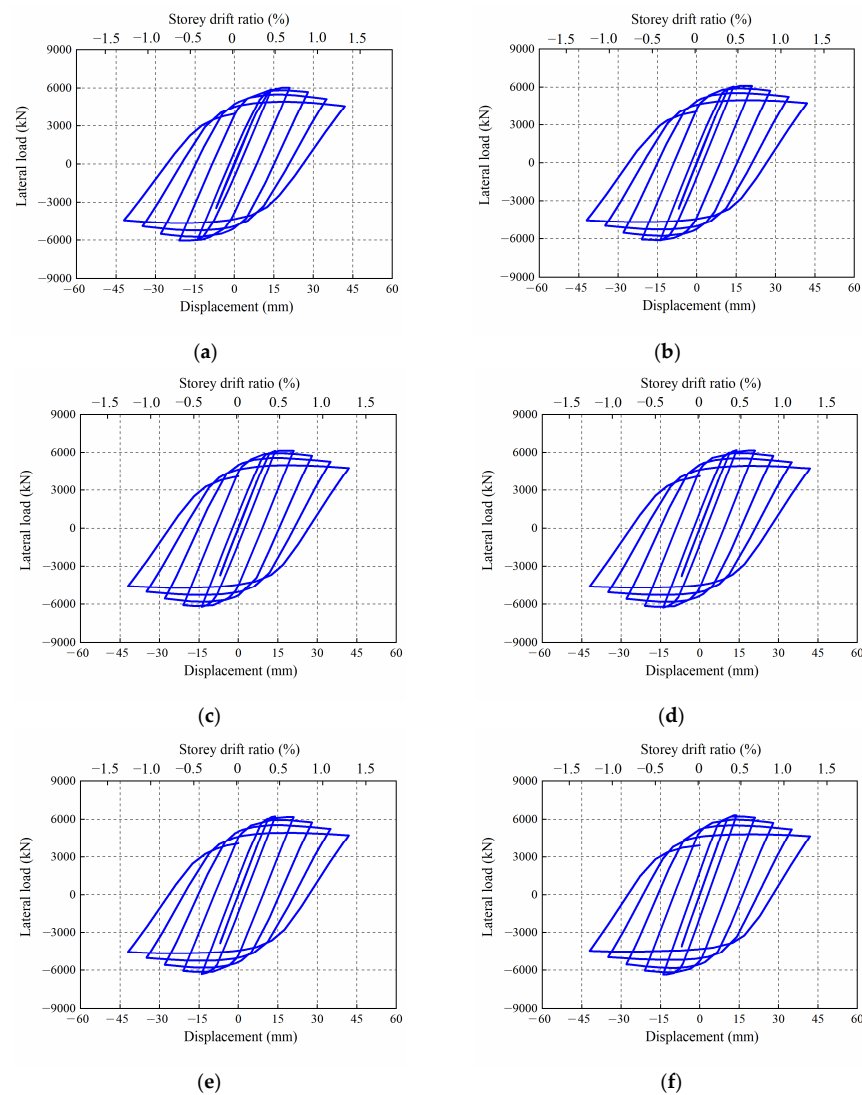


**Figure 25.** Hysteretic curves of CboSPSWs with different surrounding beam stiffnesses. (a)  $I_b = 0.25I_{b\min}$ ; (b)  $I_b = 0.50I_{b\min}$ ; (c)  $I_b = 0.75I_{b\min}$ ; (d)  $I_b = 1.0I_{b\min}$ ; (e)  $I_b = 2.0I_{b\min}$ ; (f)  $I_b = 10.0I_{b\min}$ .

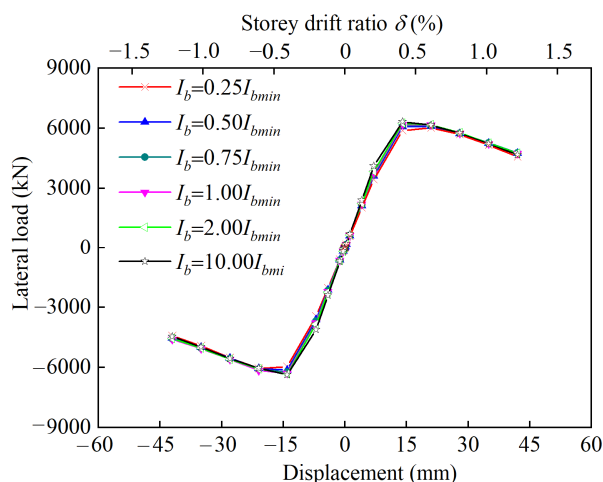


Figure 26. Skeleton curves of CboSPSWs with different surrounding beam stiffnesses.

Figures 25 and 26 show that the shapes of the CboSPSWs were fuller as the stiffness of the surrounding beams increased. The initial stiffness and shear strength increased with increases in the surrounding beam stiffness. When the surrounding beam stiffness reached  $0.25I_{bmin}$ , the ultimate strength of the CSPs in the CboSPSWs tended to be stable. The stiffness requirements of the surrounding beams were less than those of the FSPSWs. In addition, the energy dissipation coefficient of the CSPs increased with increases in the surrounding beam stiffness, as shown in Figure 27.

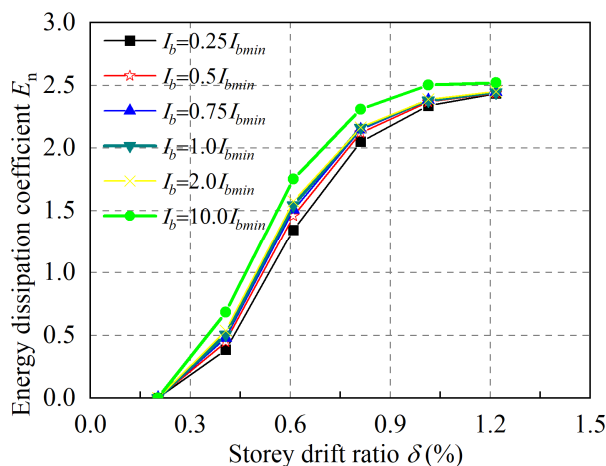
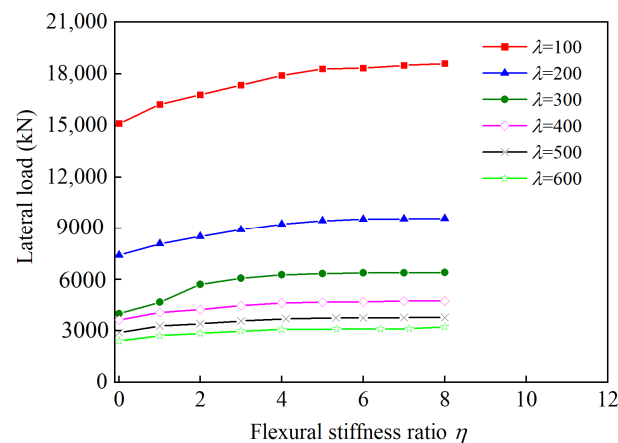


Figure 27. Energy dissipation coefficients of CboSPSWs with different surrounding beam stiffnesses.

#### 4. Limit of the Stiffness of the Free-Edge Stiffeners

According to Section 3.4, the stiffness of the free-edge stiffener plays an important role in the ultimate load and the development of the tension field in the CSP. As the stiffeners of the infilled plates, free-edge stiffeners should have enough out-of-plane stiffness and strength to provide enough boundary constraints for CSPs. Given this, the limits of the stiffness of the free-edge stiffeners of CboSPSWs with different geometric parameters were investigated.

In order to determine the limits of the stiffness of the free-edge stiffeners of CboSPSWs, a series of CboSPSWs with different height–thickness ratios were developed. In these models, the height–thickness ratio varied from 100 to 600. The CSP heights and widths were all 3000 mm. The section sizes of the surrounding columns and columns were HW-600 mm × 600 mm × 60 mm × 60 mm. The curves of the ultimate loads of CSPs versus the flexural stiffness ratio  $\eta$  are shown in Figure 28.



**Figure 28.** Curves of ultimate load versus flexural stiffness ratio.

Therefore, the limit of the stiffness of the free-edge stiffeners can be obtained as:

$$\eta = \frac{2E_s I_s}{D_x H_w} \geq 1.0 \quad (5)$$

$$I_s = \frac{1}{12} t_s b_s^3 \quad (6)$$

$$D_x = \frac{E_w}{12} B t_w^3 + \sum E_w B t_w \left(\frac{h_r}{2}\right)^2 + \sum \frac{E_w}{12} t_w h_r^3 \quad (7)$$

In Figure 28, the ultimate loads of the tension fields formed in CSPs increased with increases in the flexural stiffness ratio  $\eta$ . As the stiffeners of infilled plates, the loading mechanisms of free-edge stiffeners were affected the surrounding columns in FSPSWs. Therefore, the stiffness limits of the free-edge stiffeners can be determined according to the analysis method of the stiffness limits of the surrounding columns in FSPSWs [36]. When the increases in the average stress of the CSPs close to the beams were less than 20%, the stiffnesses of the edge stiffeners increased. The curves of the shear loads of CSPs close to the beams versus the flexural stiffness ratio are shown in Figure 28. The shear loads of the CSPs close to the beams in the CboSPSWs with no stiffeners were 15, 125, 7418, 4110, 3647, 2887, and 2409 kN, respectively, when the height–thickness ratios  $\lambda$  were 100, 200, 300, 400, 500, and 600. The shear loads of the CSPs close to the beams in the CboSPSWs with flexural stiffness ratios  $\eta = 1.0$  increased to 16026, 8081, 4679, 4063, 3273, and 2721 kN, respectively, when the height–thickness ratios  $\lambda$  were 100, 200, 300, 400, 500, and 600. It is shown that increases of the shear loads were less than 20% with increases in the edge stiffness, and the ultimate loads of the CSPs tended to be stable, as shown in Figure 28. It is suggested that the flexural stiffness ratio  $\eta$  should be greater than 1.0 in the design of free-edge stiffeners in the CboSPSWs.

Besides the constraints for the tension field, the free-edge stiffeners should have enough strength. A study in the literature [27] investigated the minimum sectional areas of the free-edge stiffeners according to the strength requirements of the CSPs, which were obtained via the mechanical equilibrium equations in Figure 20, and the minimum sectional area of a free-edge stiffener  $A_s$  can be expressed as [27]:

$$A_s = \frac{\tau_y t_w H_w}{2 f_{ys}} \quad (8)$$

where  $f_{ys}$  is the yield stress of the free-edge stiffener.

## 5. Analysis Method for a CboSPSW Based on PFI

The above plastic analyses for CboSPSWs are time-consuming, difficult, and complex. The Plate–Frame Interaction model (PFI) [36] provides convenient insights into the funda-

mental features of the seismic analyses of shear walls, including the buckling strength, yield displacement, yield load, ultimate load, and displacement corresponding to the ultimate load. The overall mechanical properties of CboSPSWs can be obtained by superposing the mechanical properties of the frames and CSPs in the CboSPSWs.

When the free-edge stiffeners have enough strength and stiffness, the mechanical properties of the CSPs in CboSPSWs are consistent with those of CbcSPSWs (CSPs connected with beams and columns).

The buckling load of a CSP  $V_{cr}$  can be obtained as:

$$V_{cr} = \tau_{cr} B t_w \quad (9)$$

where  $\tau_{cr}$  is the buckling stress of the CSP.

The buckling stress of the CSP  $\tau_{cr}$  can be obtained as [15]:

$$\frac{\tau_{cr}}{\tau_y} = \begin{cases} 1 & \lambda_s < 0.6 \\ 1 - 0.614(\lambda_s - 0.6) & 0.6 \leq \lambda_s < \sqrt{2} \\ 1/\lambda_s^2 & \lambda_s \geq \sqrt{2} \end{cases} \quad (10)$$

$$\lambda_s = \left( \tau_y / \tau_{cr}^E \right)^{0.5} \quad (11)$$

where  $\lambda_s$  is the slenderness ratio of the CSP,  $\tau_{cr}^E$  is the elastic buckling stress of the CSP,  $\tau_y$  is yield stress of the CSP.

The elastic buckling stress of the CSP  $\tau_{cr}^E$  can be expressed as [37,38]:

$$\tau_{cr}^E = \frac{\tau_{cr,G}^E \times \tau_{cr,L}^E}{\tau_{cr,G}^E + \tau_{cr,L}^E} \quad (12)$$

$$\tau_{cr,L}^E = [5.34 + 4\left(\frac{b}{B}\right)^2] \frac{\pi^2 E_w}{12(1 - \mu^2)} \left(\frac{t_w}{b}\right)^2 \quad (13)$$

$$\tau_{cr,G}^E = 36\beta E_w \frac{1}{12(1 - \mu^2)^{1/4}} \left( \frac{\left(\frac{h_r}{t_w}\right)^2 + 1}{6\eta_w} \right)^{3/4} \left(\frac{t_w}{B}\right)^2 \quad (14)$$

where  $\tau_{cr,L}^E$  and  $\tau_{cr,G}^E$  are the elastic local and global buckling stresses of the CSP,  $\tau_{cr}^E$  is the first-order buckling stress of the CSP,  $\beta$  is global buckling coefficient of the CSP,  $\eta_w$  is strength reduction factor of the CSP, and  $\mu$  is the Poisson ratio of the CSP material.

The initial stiffness of the CSPs in CboSPSWs  $K_c$  can be expressed as [35]:

$$K_c = \varphi K_w \quad (15)$$

$$\varphi = 0.014 \ln(B/H_w) - 0.118 \ln(\lambda) + 1.24 \quad (16)$$

$$K_w = \frac{GBt_w}{H_w} \quad (17)$$

where  $G$  is the shear modulus of the CSP,  $K_w$  is the initial stiffness of the CSP, and  $\varphi$  is the reduction factor for the initial stiffness of the CSP due to the initial imperfection of the CSP.

The initial stiffness of CboSPSWs can be obtained as:

$$K = K_c + 24 \frac{E_f I_f}{H_b} \quad (18)$$

where  $E_f$  is the elastic modulus of the surrounding column and  $I_f$  is the cross-sectional moment of inertia of the column.

Then, the buckling displacement of the CboSPSWs  $\Delta_{cr}$  can be calculated as:

$$\Delta_{cr} = \frac{V_{cr}(K_c + K_f)}{K_c^2} \quad (19)$$

The ultimate load of the CSPs in CboSPSWs  $V_u$  can be obtained as [22]:

$$V_u = (\tau_{cr} + 0.5\sigma_{ty} \sin 2\alpha) Bt_w \quad (20)$$

The displacements corresponding to the ultimate loads of CboSPSWs can be calculated as:

$$\Delta_u = \left( \frac{\tau_{cr}}{G} + \frac{2\sigma_{ty}}{E_w \sin 2\alpha} \right) H_w \quad (21)$$

Figure 29 provides a comparison of the load–displacement curves between the FE models ( $\lambda = 200$  and 500) and PFI models. From Figure 29, the ultimate load ratio of the PFI model ( $\lambda = 200$ ) to the FE model ( $\lambda = 200$ ) was 1.05, and the displacement corresponding to ultimate load ratio of the former one to the latter one was 0.92. In the CboSPSW ( $\lambda = 500$ ), the ultimate load ratio of the PFI model ( $\lambda = 500$ ) to the FE model ( $\lambda = 500$ ) was 1.12, and the displacement corresponding to ultimate load ratio of the former one to the latter one was 0.94. The results show that the PFI models can effectively predict the initial stiffness and ultimate loads of CboSPSWs, which can be used in the design and plastic analyses of CboSPSWs.

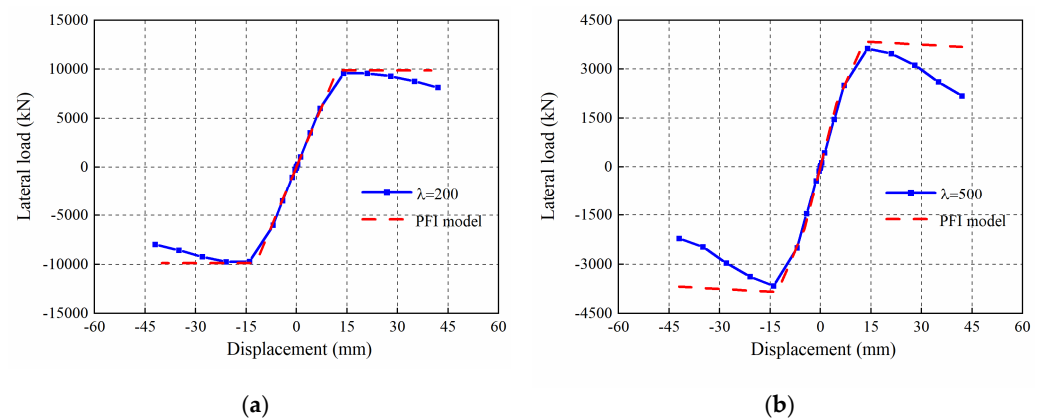


**Figure 29.** Comparisons of load–displacement curves between FE and PFI models. (a)  $\lambda = 200$ ; (b)  $\lambda = 500$ .

## 6. Conclusions

This paper investigated the seismic performance of CboSPSWs using numerical simulations. The effects of key parameters on the hysteretic performance of the CboSPSWs were studied, including the height–thickness ratio, aspect ratio, corrugation angle, stiffnesses of free-edge stiffeners, and surrounding frame stiffness. In addition, the limit of the stiffness of the free-edge stiffener in CboSPSWs was proposed, and the analysis method for CboSPSWs was examined. The main conclusions are as follows:

(1) The ultimate load, initial stiffness, and energy dissipation increase with increases in the height–thickness ratio. When the height–thickness ratio reaches 700, the energy dissipation capacity of the CSP decreases significantly. It is suggested that the height–thickness ratio should be less than 600 in the design and application of CboSPSWs for stable energy dissipation. The suitable range of corrugation angles of CSPs is from  $45^\circ$  to  $60^\circ$ .

(2) The stiffness of the free-edge stiffener has a significant impact on the strength and development of the tension field. Due to the low efficiency shear zones distributed in the areas the near the free edges, the mechanical properties of the CSPs in the CboSPSWs with no stiffeners are not fully utilized, and the tension field of the CSPs cannot develop

fully. The ultimate strength of the CSP increases with increases in the stiffness of the edge stiffener. The ultimate loads of the CboSPSWs with free-edge stiffeners were improved by 14–30% compared to those without free-edge stiffeners.

(3) The limit of the stiffness of the free-edge stiffeners can be obtained using the flexural stiffness ratio  $\eta$ . When the flexural stiffness ratio  $\eta$  exceeds 1.0, the average stress of the CSPs close to the beams was less than 20%, and the tension field develops fully in the CSPs in CboSPSWs. It is suggested that the flexural stiffness ratio  $\eta$  should be greater than 1.0 in the design of free-edge stiffeners in the CboSPSWs.

(4) The PFI model can effectively predict the shear strength and initial stiffness of CboSPSWs with good accuracy, and the PFI model can be used in the design and plastic analyses of CboSPSWs.

This paper investigates the seismic performance of the CboSPSW, and more cyclic loading tests of CboSPSWs are essential. Besides this, the artificial intelligence methods provide new sights for the static and seismic performances of CboSPSWs.

**Author Contributions:** Q.C., software, finite element analysis, writing—original draft preparation, writing—review and editing; J.H., methodology, resources, supervision, project administration, funding acquisition; B.G., project administration, software. All authors have read and agreed to the published version of the manuscript.

**Funding:** This work is supported by the National 13th Five-Year Science and Technology Support Program of China, grant No: 2016YFB1200602. Their support is acknowledged with thanks.

**Data Availability Statement:** Not applicable.

**Conflicts of Interest:** The authors declare no conflict of interest.

## Abbreviations

List of symbols/abbreviations:

$A_s$	Minimum sectional area of a free-edge stiffener
$b$	Horizontal subpanel width of the CSP
$B$	Width of the CSP
$B_c$	Center distance between adjacent columns
$d$	Horizontal projection of inclined subpanel width
$D_x$	Sectional moment of inertia of the CSP
$E_n$	Energy dissipation coefficients of the CSP
$E_w$	Elastic modulus of the CSP
$E_f$	Elastic modulus of the surrounding column
$I_f$	Cross-sectional moment of inertia of the column.
$\Delta_{cr}$	Buckling displacement of the CboSPSW
$E_s$	Elastic modulus of the free free edge
$f_{ys}$	Yield stress of a free-edge stiffener
$h_r$	Corrugation depth of the CSP
$H$	CSP height
$H_b$	Center distance between adjacent beams
$I_s$	Moment of inertia of the free-edge stiffener
$I_{bmin}$	Minimum area moment of inertia of the surrounding beam
$K_c$	Initial stiffness of the CSP
$\varphi$	Reduction factor for the initial stiffness of the CSP
$K_c$	Initial stiffness of the CSP
$K$	Initial stiffness of CboSPSWs
$t_w$	Thickness of the CSP
$V_{cr}$	Buckling load of a CSP
$V_u$	Ultimate load of the CSP
$\Delta_y$	Yield displacement of the CSP

$\Delta_u$	Displacement corresponding to the ultimate load
$\mu$	Ductility coefficient
$\theta$	Corrugation angle
$\alpha$	Inclination angle of the tension field in the CSP
$\eta$	Flexural stiffness ratio of the stiffener of the free edge
$\lambda$	Height-thickness ratio of the CSP
$\lambda_s$	Slenderness ratio of the CSP
$\tau_{cr}^E$	Elastic buckling stress of the CSP
$\tau_{cr}^E$	Elastic buckling stresses of the CSP
$\tau_{cr,G}^E$	Elastic global buckling stresses of the CSP
$\tau_y$	Yield stress of a corrugated steel plate
$\tau_{cr}$	Buckling stress of the CSP
$G$	Shear modulus of the CSP

## References

1. Sabelli, R.; Bruneau, M. *AISC Steel Design Guide 20: Steel Plate Shear Walls*; American Institute of Steel Construction: Chicago, IL, USA, 2007.
2. Jin, S.; Yang, S.; Bai, J. Numerical and experimental investigation of the full-scale buckling-restrained steel plate shear wall with inclined slots. *Thin-Walled Struct.* **2019**, *144*, 106362. [[CrossRef](#)]
3. Mu, Z.; Yang, Y. Experimental and numerical study on seismic behavior of obliquely stiffened steel plate shear walls with openings. *Thin-Walled Struct.* **2020**, *146*, 106457. [[CrossRef](#)]
4. Nezamisavojbolaghi, K.; Gharani, A. Numerical Study on Stiffened Steel Plate Shear Walls with Central Perforation. In Proceedings of the 6th International Conference on Computational Methods in Structural Dynamics and Earthquake Engineering Methods in Structural Dynamics and Earthquake Engineering, Rhodes Island, Greece, 15 June 2017.
5. Haddad, O.; Sulong, N.; Ibrahim, Z. Cyclic performance of stiffened steel plate shear walls with various configurations of stiffeners. *J. Vibroeng.* **2018**, *20*, 459–476. [[CrossRef](#)]
6. Edalati, Y.; Yadollahi, S. Numerical study on the performance of corrugated steel shear walls. *Wind Struct.* **2014**, *19*, 405–420. [[CrossRef](#)]
7. Farzampour, A. Innovative Structural Fuse Systems for Various Prototype Applications. *Materials* **2022**, *15*, 805. [[CrossRef](#)] [[PubMed](#)]
8. Luo, Q.; Wang, W.; Sun, Z.; Xu, S.; Wang, B. Seismic performance analysis of corrugated-steel-plate composite shear wall based on corner failure. *J. Constr. Steel Res.* **2021**, *180*, 106606. [[CrossRef](#)]
9. Shariati, M.; Lagzian, M.; Maleki, S.; Shariati, A.; Trung, N.T. Evaluation of seismic performance factors for tension-only braced frames. *Steel Compos. Struct. Int. J.* **2020**, *35*, 599–609.
10. Huang, Z.; Yin, Z.; Song, B. Study on seismic behaviour of trapezoidal corrugated steel plate shear wall structure with pec column. *Adv. Steel Constr.* **2023**, *19*, 157–165.
11. Farzampour, A.; Mansouri, I.; Lee, C.; Sim, H.-B.; Hu, J.W. Analysis and design recommendations for corrugated steel plate shear walls with a reduced beam section. *Thin-Walled Struct.* **2018**, *132*, 658–666. [[CrossRef](#)]
12. Zhang, W.; Mandavian, M.; Yu, C. Lateral strength and deflection of cold-formed steel shear walls using corrugated sheathing. *J. Constr. Steel Res.* **2018**, *148*, 399–408. [[CrossRef](#)]
13. Dou, C.; Pi, Y.; Gao, W. Shear resistance and post-buckling behavior of corrugated panels in steel plate shear walls. *Thin-Walled Struct.* **2018**, *131*, 816–826. [[CrossRef](#)]
14. Farzampour, A.; Mansouri, I.; Jong, W. Seismic behavior investigation of the corrugated steel shear walls considering variations of corrugation geometrical characteristics. *Int. J. Steel Struct.* **2018**, *18*, 1297–1305. [[CrossRef](#)]
15. Yi, J.; Gil, H.; Youm, K.; Lee, H. Interactive shear buckling behaviour of trapezoidally corrugated steel webs. *Eng. Struct.* **2008**, *30*, 1659–1666. [[CrossRef](#)]
16. Emami, F.; Mofid, M.; Vafai, A. Experimental study on cyclic behaviour of trapezoidally corrugated steel shear walls. *Eng. Struct.* **2013**, *48*, 750–762. [[CrossRef](#)]
17. Hosseinzadeh, L.; Mofid, M.; Aziminejad, A.; Emami, F. Elastic interactive buckling strength of corrugated steel shear wall under pure shear force. *Struct. Des. Tall Spec. Build.* **2017**, *26*, e1357. [[CrossRef](#)]
18. Cao, Q.; Huang, J.; Zhao, L.; Fang, Z.; Zhang, Z. Research on shear performance of corrugated steel plate shear walls with inelastic buckling of infilled plates under lateral loads. *J. Build. Eng.* **2022**, *52*, 104406. [[CrossRef](#)]
19. Zhao, Q.; Qiu, J.; Zhao, Y.; Cheng, Y. Performance-Based Seismic Design of Corrugated Steel Plate Shear Walls. *KSCE J. Civ. Eng.* **2022**, *26*, 3486–3503. [[CrossRef](#)]
20. Zhao, Q.; Qiu, J.; Li, N.; Li, Z. Experimental study on seismic performance of trapezoidally corrugated steel plate shear walls. *J. Build. Struct.* **2018**, *39*, 112–120.
21. Tong, J.; Guo, Y. Elastic buckling behavior of steel trapezoidal corrugated shear walls with vertical stiffeners. *Thin-Walled Struct.* **2015**, *95*, 31–39. [[CrossRef](#)]
22. Farzampour, A.; Laman, J.A.; Mofid, M. Behavior prediction of corrugated steel plate shear walls with openings. *J. Constr. Steel Res.* **2015**, *114*, 258–268. [[CrossRef](#)]

23. Huang, S. Experimental Study on Seismic Behavior of Corrugated Steel Shear Walls. Ph.D. Thesis, Xi'an University of Architecture and Technology, Xi'an, China, 2019. (In Chinese).
24. Dou, C.; Xie, Z.; Yang, N. Lateral resistance and optimized design of embedded panels in folded steel plate walls with vertical connections on both sides. *Eng. Mech.* **2022**, *39*, 60–67. (In Chinese)
25. Chen, B.; Guo, Y.; Zuo, J.; Zhao, X.-Y. Strength design of prefabricated corrugated steel plate shear walls under combined compression and shear loads. *J. Build. Eng.* **2023**, *65*, 105790.
26. Feng, L.; Sun, T.; Ou, J. Elastic buckling analysis of steel-strip-stiffened trapezoidal corrugated steel plate shear walls. *J. Constr. Steel Res.* **2021**, *9*, 184. [[CrossRef](#)]
27. Zhao, Q.; Qiu, J.; Hao, B.; Wang, Q. Lateral behaviour of vertically-corrugated Steel plate shear walls connected with beams only. *J. Tianjin Univ.* **2019**, *2*, 46–53.
28. Qiu, M. Seismic Performance Analysis of Corrugated Steel Plate Shear Wall Connected at Both Sides. Master's Thesis, Dalian University of Technology, Dalian, China, 2020.
29. Sun, J.; Ma, Y.; Li, J.; Zhang, J.; Ren, Z.; Wang, X. Machine learning-aided design and prediction of cementitious composites containing graphite and slag powder. *J. Build. Eng.* **2021**, *43*, 102544. [[CrossRef](#)]
30. Sun, J.; Ma, Y.; Li, J.; Zhang, J.; Xiao, F.; Sun, Y.; Ren, Z.; Zhang, G.; Liu, S.; Wang, Y. Multi-objective optimisation of a graphite-slag conductive composite applying a BAS-SVR based model. *J. Build. Eng.* **2021**, *44*, 103223. [[CrossRef](#)]
31. Feng, W.; Wang, Y.; Sun, J.; Tang, Y.; Wu, D.; Jiang, Z.; Wang, J.; Wang, X. Prediction of thermo-mechanical properties of rubber-modified recycled aggregate concrete. *Constr. Build. Mater.* **2022**, *318*, 125970. [[CrossRef](#)]
32. Zhang, J.; Sun, Y.; Li, G.; Wang, Y.; Sun, J.; Li, J. Machine-learning-assisted shear strength prediction of reinforced concrete beams with and without stirrups. *Eng. Comput.* **2020**, *38*, 1293–1307. [[CrossRef](#)]
33. Sun, J.; Wang, J.; Zhu, Z.; He, R.; Peng, C.; Zhang, C.; Huang, J.; Wang, Y.; Wang, X. Mechanical Performance Prediction for Sustainable High-Strength Concrete Using Bio-Inspired Neural Network. *Buildings* **2022**, *12*, 65. [[CrossRef](#)]
34. Li, N. Experimental Research on Seismic Behavior of Corrugated Steel Plate Shear Wall System. Master's Thesis, Tianjin University, Tianjin, China, 2016.
35. *JGJ/T 380-2015*; Technical Specification for Steel Plate Shear Walls. China Ministry of Construction: Beijing, China, 2015. (In Chinese)
36. Montgomery, C.; Medhekar, M.; Lubell, A.; Prion, H.G.L.; Ventura, C.E.; Rezai, M. Unstiffened steel plate shear wall performance under cyclic loading. *Struct. Eng.* **2001**, *127*, 973–975. [[CrossRef](#)]
37. Bergfelt, A.; Leiva, L. *Shear Buckling of Trapezoidally Corrugated Girders Webs*; Report Part 2. Pibl.SS4:2; Chalmers University of Technology: Gothenburg, Sweden, 1984.
38. Easley, J.; McFarland, D. Buckling of light-gage corrugated metal shear diaphragms. *Struct. Div.* **1969**, *95*, 3004–3006. [[CrossRef](#)]

**Disclaimer/Publisher's Note:** The statements, opinions and data contained in all publications are solely those of the individual author(s) and contributor(s) and not of MDPI and/or the editor(s). MDPI and/or the editor(s) disclaim responsibility for any injury to people or property resulting from any ideas, methods, instructions or products referred to in the content.